The Journal of Chemical Physics

RESEARCH ARTICLE | SEPTEMBER 03 2025

A refined atomistic model of functionalized self-assembled monolayers on gold: Assessment of force field parameters

Special Collection: 2025 JCP Emerging Investigators Special Collection

Cauê P. Souza ; Alexey V. Verkhovtsev ; Nigel J. Mason ; Andrey V. Solov'yov ; Felipe Fantuzzi

J. Chem. Phys. 163, 094704 (2025)
https://doi.org/10.1063/5.0274290

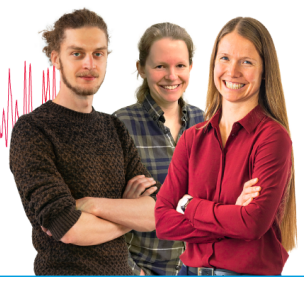

The Journal of Chemical Physics ARTICLE pubs.aip.org/aip/jcp

A refined atomistic model of functionalized self-assembled monolayers on gold: Assessment of force field parameters

Cite as: J. Chem. Phys. 163, 094704 (2025); doi: 10.1063/5.0274290
Submitted: 4 April 2025 • Accepted: 29 June 2025 •
Published Online: 3 September 2025

Cauê P. Souza,[1,a] Alexey V. Verkhovtsev,[2] Nigel J. Mason,[3] Andrey V. Solov'yov,[2] and Felipe Fantuzzi[1,b]

AFFILIATIONS

[1] Chemistry and Forensic Science, School of Natural Sciences, University of Kent, Park Wood Rd, Canterbury CT2 7NH, United Kingdom
[2] MBN Research Center, Altenhöferallee 3, 60438 Frankfurt am Main, Germany
[3] Physics and Astronomy, School of Engineering, Mathematics and Physics, University of Kent, Park Wood Rd, Canterbury CT2 7NH, United Kingdom

Note: This paper is a part of the 2025 JCP Emerging Investigators Special Collection.
[a] **Author to whom correspondence should be addressed:** cp692@kent.ac.uk
[b] **Electronic mail:** f.fantuzzi@kent.ac.uk

ABSTRACT

Self-assembled monolayers (SAMs) of alkanethiols on gold surfaces are important for various technological applications, such as electroanalytical sensors, organic electronic devices, and catalysts. However, providing a consistent computational description of the unique structural features of these SAMs, such as adsorption patterns, chain conformations, and superlattice arrangements, is challenging, particularly within a versatile computational framework that can simulate both the structural features of these systems and their irradiation-driven chemical transformations. This study systematically analyzes molecular mechanics force field parameters for bonded and nonbonded (van der Waals and electrostatic) interactions in alkanethiol SAMs with different terminal groups. Using structure optimization and energy decomposition analysis, we assess the impact of force field parameters on key properties, such as the equilibrium tilt angle, ligand packing density, and nanoscale structural organization. Based on this detailed benchmarking, an optimal set of force field parameters has been identified that reproduces the experimentally determined structural and energetic properties of SAMs and ensures their dynamic stability at room temperature. This provides a validated framework for simulating pristine and functionalized alkanethiol-coated substrates under thermal conditions relevant to experimental applications.

I. INTRODUCTION

Self-assembled monolayers (SAMs) are key nanoscale architectures with widespread impact on current scientific and technological landscape. Since the first report of self-assembled chemical systems,[1] SAMs have been extensively studied and used in various applications. These range from electronic devices—such as electroanalytical sensors,[2,3] biosensors,[4,5] and organic electronics[6–9]—to the control and enhancement of catalysts,[10,11] crystal nucleation,[12] and other nanotechnology applications.[13–16] Among the many types of SAMs, alkanethiols—organic molecules consisting of a hydrocarbon chain with a thiol (–SH) head-group—have been widely used because of their strong chemisorption onto metal surfaces, especially gold and silver. Functionalized alkanethiol SAMs, in which the terminal end of the hydrocarbon chain is modified with specific functional groups, have proven to be particularly robust and versatile. Since their introduction in the early 1980s,[17] these alkanethiol-based SAMs have found increasing utility in the fields mentioned above due

to their high degree of structural organization, tunable chemical functionality, and relative ease of preparation.

Recently, SAMs of alkanethiols on gold have been used as substrates for photoassisted chemical vapor deposition (PACVD), a near-room-temperature alternative to conventional CVD methods that is well suited for thermosensitive organic thin films.[18–20] The highly organized structure, controllable density, and functional versatility of SAMs make them ideal model systems for achieving selective and patterned deposition. For example, Salazar *et al.*[20] demonstrated that ruthenium-based precursors selectively adsorb on SAMs terminated with –OH and –COOH groups, but not on bare hydrocarbon chains, thus enabling a precise and area-specific coating.

Despite their importance, the accurate and predictive computational modeling of alkanethiol SAMs remains a significant challenge. In relation to PACVD, understanding the photochemistry of precursor molecules and optimizing them for specific applications also requires reliable computational models of the substrate. Such models must capture key structural features of the SAMs, such as adsorption sites, chain orientation, and intricate superlattice patterns under different conditions. However, developing an atomistic model that reproduces all the experimentally observed properties of SAMs has proven difficult, reflecting the complexity of these systems.

A fundamental structural feature of the alkanethiol ligands is their division into three distinct regions: the sulfur head-group anchoring the chain to the metal, the hydrocarbon spacer chain, and the functional terminal group [Fig. 1(a)]. In fully packed SAMs, the chains adopt an all-*anti* conformation and form a tilt angle α relative to the surface normal—approximately 30° for Au(111) and 15° for Au(100) at room temperature,[15,16,21,22] with other possible tilt angles discussed elsewhere.[22] The α angle varies with the length of the ligand chain,[23] the temperature,[21,24] and the nature of the metal surface.[15] The tilt angle maximizes interchain interactions and defines the thickness of the SAM, thereby influencing various properties.[1,15,25–29] To fully describe the ligand orientation, two additional angles are required [Fig. 1(a)]: the precession angle β, which defines the azimuthal orientation of the chain projection on the surface, and the rotation angle ω, which represents the rotation around the molecular axis **m**.

At full coverage, organized SAMs typically exhibit two key patterns.[15,16,21,22,30–32] First, the sulfur head-groups form a well-defined adsorption lattice. On Au(111), this corresponds to a hexagonal $\left(\sqrt{3}\times\sqrt{3}\right)$ R30° arrangement [solid rhombus in Fig. 1(b)] with a coverage of about 21.4 Å^2 per molecule.[30,33] Second, the relative orientations of the alkanethiol chains produce a $c(4\times2)$ superlattice pattern [dashed rectangle in Fig. 1(b)]. Although the detailed origin of the superlattice is still debated, the most compelling evidence points to differences in the ω angles of neighboring ligands.[21] For Au(100), the patterns are less conclusive; the coverage varies from 17.75 to 20.6 Å^2 per molecule,[34,35] and the exact adsorption sites of sulfur remain uncertain.[15,36] Density functional theory (DFT) studies suggest that the adsorption site on Au(111) is around the threefold fcc position,[16,21,33,37,38] while on Au(100), atop and hollow sites appear to be occupied simultaneously.[33] It

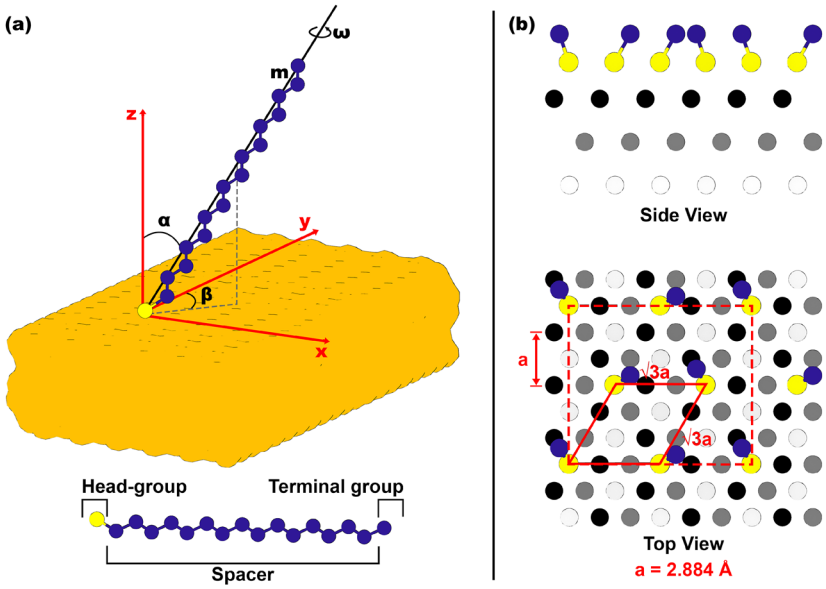

FIG. 1. Schematics of the alkanethiol SAM on Au(111). Yellow circles: sulfur; blue circles: carbon; and black, gray, and white circles: first, second, and third gold layers, respectively, from top to bottom. Hydrogens are omitted for clarity. (a) Representation of a single alkanethiol molecule adsorbed on the metal surface. Here, **m** is the molecular principal axis contained in the plane of the carbon chain in the head-group–terminal group direction. α is the ligand tilt angle, β is the precession or azimuthal angle, and ω is the rotation angle. The different regions of the ligand are indicated. (b) Representation of the hexagonal $\left(\sqrt{3}\times\sqrt{3}\right)$ R30° pattern (solid rhombus) and of the $c(4\times2)$ superlattice (dashed rectangle) formed by alkanethiol molecules on Au(111) at full coverage. The alkanethiol chains have been truncated after the first carbon atoms (attached to the sulfurs) for clarity. Notice the disposition of the angles β within a unit cell. This pattern corresponds to structure III from Zhang, Goddard, and Jiang.[21]

is also important to recognize that SAMs are not always perfectly ordered.[39–41]

Capturing this structural complexity with computational models is no small feat. Previous simulations have struggled to reproduce the experimental superlattice patterns on Au(111). For example, Sellers *et al.*[33] developed an all-atom *ab initio* force field that reproduced the ligand tilt angles and the hexagonal pattern but not the superlattice. While subsequent studies have addressed some of these aspects,[42–44] achieving stable room-temperature superlattice structures has still proven elusive. Gerdy and Goddard[45] replicated the superlattice pattern using disulfide units, and Zhang, Goddard, and Jiang[21] later succeeded by employing a Morse potential for Au–S interactions and Lennard-Jones (LJ) parameters from the Universal Force Field (UFF).[46] Despite these advances, including efforts within the ReaxFF framework,[38,47,48] a comprehensive model that accurately captures all relevant structural and energetic properties is still lacking.

In this work, we address this challenge using the advanced software package MBN Explorer[49] and its dedicated multitasking toolkit MBN Studio[50] to systematically investigate how different FF parameters—bonded terms, partial charges (and their scaling), and LJ interactions—impact the stability and structural properties of alkanethiol SAMs on Au(111) and Au(100). Central to our approach is an energy decomposition analysis, performed as a function of the ligand tilt angle, which isolates the contributions of each parameter to the overall characteristics of the SAM. By considering both pristine and functionalized alkanethiol chains—relevant, e.g., for the selective metallization of SAMs under PACVD conditions—we obtain a set of optimized FF parameters that consistently reproduce key structural features such as adsorption patterns, chain conformations, and the experimentally observed superlattice arrangements on Au(111) surfaces. We not only cover the cases of functionalized alkanethiol SAMs, which are particularly scarce in the computational literature, but we also describe a detailed procedure to extend the study of the effect of FF parameters on key properties of these systems for different ligand–surface combinations. Ultimately, this study represents an important first step toward atomistic modeling of the PACVD process. In subsequent studies, the SAMs modeled and analyzed here will be employed as representative substrates to simulate their metallization process under PACVD conditions.

II. COMPUTATIONAL METHODS

This section provides an overview of the computational methods used in this study. Further details are given in the supplementary material.

All atomistic simulations were performed using MBN Explorer,[49] which enables the combination of multiple interaction potentials and flexible FF parameterization. The aim was to develop parameters compatible with the CHARMM framework by combining directly available CHARMM data with complementary parameters from external databases. In particular, SwissParam[51,52] and the CHARMM General Force Field (CGenFF)[53–55] were employed to generate bonded and nonbonded parameters for the ligands (Fig. 2), namely, 1-hexadecanethiol (HDT^{H}), 16-hydroxy-1-hexadecanethiol (HDT^{OH}), and 16-mercaptohexadecanoic acid (HDT^{COOH}). Additional LJ parameters from the UFF[46] were tested because of their proven reliability in modeling alkanethiol SAMs on gold surfaces.[21] The criteria for selecting these sources were twofold: (1) the availability of a simple tool for extracting all necessary FF parameters, as well as geometry (PDB) and topology (PSF) files for ligand molecules in a CHARMM-compatible format; and (2) the general applicability of the dataset. Our intention was not to conduct an exhaustive survey but rather to keep the number of FF sets to a minimum while still demonstrating the capabilities of our strategy and identifying a suitable final parameter set. Here, the all-atom Optimized Potentials for Liquid Simulations (OPLS-AA) force field deserves mention.[56] While the LigParGen engine[57] allows for the extraction of FF parameters for organic molecules in CHARMM and other formats, it does not provide PSF files. Moreover, OPLS-AA has been shown to perform less reliably than alternative FFs in reproducing characteristic tilt angles of alkanethiol SAMs.[58] For these reasons, and in line with our goal of a streamlined selection, OPLS-AA was not included in the present work.

FIG. 2. Alkanethiyl structures considered in this study. The names are those of the parent thiols. White: hydrogen, blue: carbon, red: oxygen, and yellow: sulfur. Their respective abbreviations are utilized throughout this text.

The ligands were modeled as thiyl radicals formed by the abstraction of a hydrogen atom from the thiol (–SH) group. Geometry optimization of the isolated radicals was performed at the DFT level using the M06-2X functional[59] in combination with Grimme's D3 dispersion corrections[60] and the Ahlrichs def2-TZVP basis set for all atoms except sulfur, for which the def2-TZVPPD basis set was employed.[61] Vibrational frequency calculations confirmed all optimized structures as energy minima, and Natural Bond Orbital (NBO) analysis[62] provided partial charges for use in the FF parameterization. All DFT calculations were performed using Gaussian 16, Revision A.03.[63]

The gold substrates, consisting of five-layer slabs of Au(111) and Au(100), were constructed using MBN Studio.[50] The Au(111) substrate had dimensions of 59.856 ‰ × 95.172 ‰ (3960 atoms), while the Au(100) substrate had the size of 73.408 ‰ × 73.408 ‰ (3240 atoms). Au–Au interactions were described using the Finnis–Sinclair many-body potential.[64,65]

Each gold slab was initially optimized under periodic boundary conditions using the velocity quenching algorithm with a 0.1 fs time step. All tolerances were set to 10^{-6}, and the optimizations were run until these criteria were met. For all subsequent simulations, the bottom-most layer was frozen to simulate bulk crystal behavior.

Morse[21] and LJ[66] parameters for Au–S interactions were considered to account for the chemisorption of the alkanethiols onto the gold surface.

To evaluate the suitability of different FF parameterizations, we tested eight different sets that varied in their bonded parameters, partial charge values, and LJ parameters (Table I). Each FF set was assessed based on its ability to reproduce key geometrical properties of SAMs, such as the ligand tilt angle, on both the Au(111) and Au(100) surfaces. In initial geometries, ligands were arranged in a rectangular grid with target densities of 4.67 nm^{-2} [as measured experimentally for Au(111)[30]] as well as 90% of this value for both surfaces. The actual densities were 4.67 and 4.21 nm^{-2} for Au(111) and 4.73 and 4.17 nm^{-2} for Au(100). Molecular dynamics (MD) simulations with constant velocities and no interaction parameters were used to generate initial geometries by driving the ligands to different tilt angles (see the supplementary material for details). For each initial configuration and parameter set, a short geometry optimization calculation (25 000 steps) was performed to relax the systems and check their structural stability. These optimizations employed velocity quenching with a 0.01 fs time step, the linked cell algorithm[49,67] for neighbor lists, and the particle mesh Ewald (PME) algorithm for the description of electrostatic interactions. Cutoffs of 12 and 10 ‰ were used for the Coulomb and LJ interactions, respectively.

The best-performing parameter set (set **3**, see below) was further validated by constructing SAMs on Au(111) with experimentally observed sulfur-atom arrangements and superlattice patterns for all three ligands.[21] Long optimization runs (3×10^6 steps) confirmed the stability of these structures and the ability of the chosen parameter set to correctly describe the adsorption sites and tilt angles. All convergence tolerances, namely, displacement (Å), maximum displacement (Å), and force (eV/Å), were set to 10^{-6}. These thresholds were not reached by the end of the 3 000 000 optimization cycles. The remaining optimization parameters were the same as described above. We analyzed the ligand tilt angle α, precession angle β, and rotation angle ω [Fig. 1(a)] frame by frame. The angle α was defined relative to the z-axis, normal to the surface; β was defined relative to the y-axis, which is aligned with the surface lattice vector; ω was defined as the angle between the plane containing the carbon atoms in the chain and the plane formed by the z-axis and the molecular axis **m** [Fig. 1(a)]. While α is unsigned, β and ω range from −180° to 180°, with counterclockwise angles being considered positive. The top four carbon atoms of each ligand and the ligands crossing the simulation box boundaries were excluded from the analysis. This angle analysis was performed by a custom-built Python script using MDTraj[68] and Matplotlib.[69]

Finally, trial MD simulations were performed starting from the final optimized geometry for the HDT^H SAM on Au(111), using the selected force field parameter set. The system was simulated for 10 ns at 300 K, with a time step of 1 fs. A Langevin thermostat with a damping time of 100 fs was applied. Charge damping factors ranging from 0.0 to 1.0 in steps of 0.1 were applied to fine-tune the partial charges, followed by a refinement in steps of 0.025 once an optimum value was identified (see Sec. III G). All other simulation parameters were the same as for the optimizations described above.

III. RESULTS AND DISCUSSION

This section is organized as follows: In Sec. III A, we assess different force field sets by comparing the geometries of isolated alkanethiol ligands with DFT references to establish an initial benchmark. Section III B then explores how nonbonded parameters, particularly the interplay between electrostatic and van der Waals interactions, affect the ligand tilt angle. In Sec. III C, we focus on tilt angle analysis for SAMs on Au(111), considering different charge damping factors, while Sec. III D extends this investigation to Au(100). Secs. III E and III F discuss how coverage density and ligand arrangement influence the geometry and energetics of SAMs. Finally, Sec. III G reports on the fine-tuning of partial charges that ensures stability of the system upon 300 K MD simulations, thus yielding the final FF parameter set.

A. Initial force field assessment with isolated ligands

As an initial evaluation of the quality of each FF set, we conducted a detailed comparison of the MM-optimized geometries of the three thiyl radicals—1-hexadecanethiol (HDT^H), 16-hydroxy-1-hexadecanethiol (HDT^{OH}), and 16-mercaptohexadecanoic acid (HDT^{COOH})—with their corresponding geometries obtained by DFT optimization. The RMSD values for the MM- and DFT-optimized geometries are listed in Table II. This comparison provides an important basis for evaluating the parameterization quality of the selected FF combinations and their ability to reproduce reliable molecular geometries.

TABLE I. Nomenclature and composition of the different force field sets tested in this work. MMFF was obtained from SwissParam.

Set	Bonded	Partial charges	Lennard-Jones
1	CGenFF	CGenFF	CGenFF
2	CGenFF	NBO	CGenFF
3	CGenFF	CGenFF	UFF
4	CGenFF	NBO	UFF
5	MMFF	CGenFF	MMFF
6	MMFF	NBO	MMFF
7	MMFF	CGenFF	UFF
8	MMFF	NBO	UFF

TABLE II. Comparison between MM- and DFT-optimized geometries as RMSD (Å) for each FF set (see Table I) for the three ligands (as thiyl radicals) considered. HDT^H: 1-hexadecanethiol, HDT^{OH}: 16-hydroxy-1-hexadecanethiol, and HDT^{COOH}: 16-mercaptohexadecanoic acid.

Set	HDT^H	HDT^{OH}	HDT^{COOH}
1	0.241	0.252	0.359
2	0.237	0.253	0.365
3	0.239	0.251	0.165
4	0.236	0.253	0.203
5	1.487	1.480	0.467
6	1.482	1.489	1.128
7	1.482	1.486	0.361
8	1.479	1.484	0.390

The data show a consistent trend: SwissParam (MMFF, sets **5–8**) generally underperforms compared to CGenFF (sets **1–4**) for all three ligands, with the RMSD values for SwissParam being up to six times higher. This discrepancy is most evident for HDT^{H} and HDT^{OH}, while for HDT^{COOH}, the differences between the two FF sources are somewhat mitigated. This observation suggests that the inherent parameterization approach used in MMFF may not be as robust as that of CGenFF, especially for complex or functionalized ligands.

As expected, nonbonded interactions play a relatively minor role in determining the optimized geometries of isolated molecules, whose structures are mainly governed by bonded parameters. Nevertheless, slight improvements were observed when LJ parameters from UFF were employed (sets **3**, **4**, **7**, and **8**). These improvements are particularly noticeable for HDT^{COOH}, where UFF parameters give slightly better agreement with DFT geometries than those derived from CGenFF or SwissParam. For HDT^{H} and HDT^{OH}, the differences introduced by the choice of LJ parameters are negligible, evidencing the limited influence of these parameters in the absence of intermolecular interactions.

The choice of partial charge assignment—whether from CGenFF or derived using NBO analysis—also influences the geometry optimization results. Overall, CGenFF charges exhibit superior performance compared to NBO-derived charges, particularly for HDT^{COOH}. This difference is likely to be due to the greater compatibility of CGenFF charges with the CHARMM FF framework, which ensures better parameter synergy during MM optimization. For HDT^{H}, the RMSD values are comparable regardless of the charge source, suggesting a reduced sensitivity to partial charges for simpler alkanethiols.

The performance of the FF combinations tested in this work varies, with sets **1–4** offering reasonable accuracy in reproducing DFT geometries. Among these, set **3** demonstrates the best overall performance, achieving a consistent balance between the contributions of the bonded and nonbonded parameters. The superiority of set **3** is particularly evident in its handling of HDT^{COOH}, where the interplay between the carboxyl terminal group and the rest of the molecule requires a more nuanced parameterization.

B. Evaluating the effect of nonbonded parameters

While the bonded parameters primarily define the molecular geometry of each alkanethiol chain, the nonbonded parameters are expected to play a more significant role in influencing the overall morphology of the SAMs. To evaluate this effect, the behavior of the ligand tilt angle α [Fig. 1(a)] was investigated for different FF parameter sets. This assessment was performed by energy scans of α, incorporating a homogeneous partial charge damping factor to investigate the interplay between the Coulomb and van der Waals interactions.

For each angle–charge damping combination, we performed short geometry optimizations, selecting specific optimization steps to plot the resulting energies (see the supplementary material for detailed protocols). The provided scans highlight how the FF parameters influence the stability and preferred configurations of the SAMs.

A comprehensive analysis of the energy components contributing to the total system energy was performed, focusing on their dependence on the ligand tilt angle α. For clarity and brevity, Fig. 3 shows the results for two representative systems, both corresponding to HDT^{H} SAMs on Au(100). The first system (top panel) was simulated using the FF parameter set **1**, while the second (bottom panel) was simulated using set **3**. The total energy for the system is the sum of all (i) bonded (bond, angle, and dihedral) and (ii) nonbonded (Coulomb and van der Waals) interactions defined by the CHARMM parameters, as well as (iii) the Au–S Morse bonded interaction (included in the "pairwise" contribution along with the LJ interactions) and (iv) the Finnis–Sinclair many-body potential between the Au atoms (this last contribution, which is nearly constant, is not shown in the plots). The complete dataset is presented in the supplementary material.

The total energy profile for set **1** shows a minimum at a tilt angle below 10°, followed by a sharp increase in energy as α grows. This behavior is predominantly driven by Coulomb repulsion, indicating that electrostatic interactions are a critical factor for this FF configuration. At first sight, one might infer that the partial charges in set **1** are poorly parameterized and cause the system to stabilize at smaller α angles. However, if we compare the energy profile of

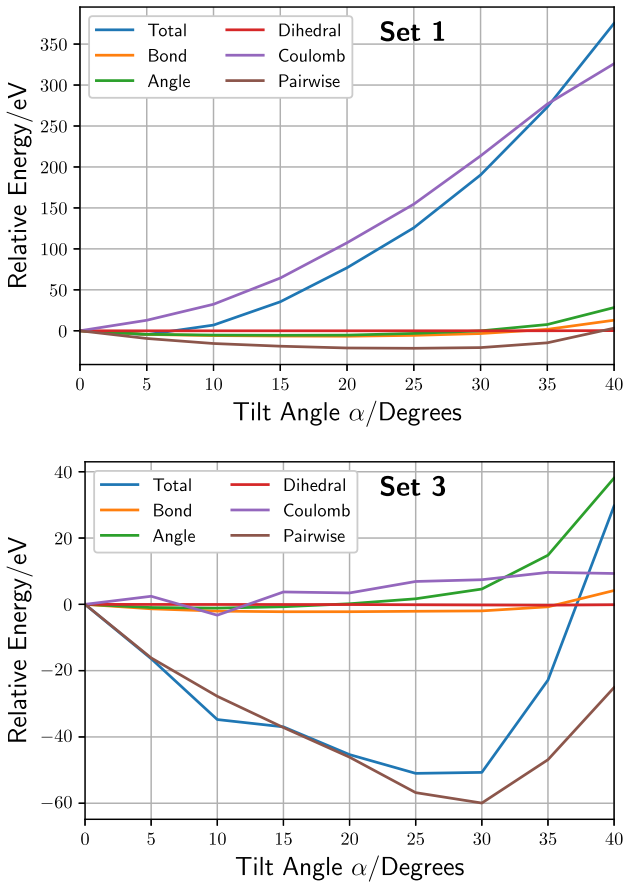

FIG. 3. Energy decomposition analysis as a function of ligand tilt angle for FF parameter sets **1** and **3** for HDT^{H} on Au(100) with a density of 4.17 nm^{-2}. For each component, the relative energy is referenced to the respective value at 0°.

set **1** with that of set **3**, which differ only in the choice of LJ parameters (Table I), the data for set **3** show that LJ interactions, rather than Coulomb forces, are the primary determinants of the energy dependence. The pairwise interaction component, which included both LJ and the Au–S Morse potential, drives the stabilization. Since the Au–S bonded interaction remains constant after sufficient optimization, it is evident that the variation of the LJ interactions determines these differences.

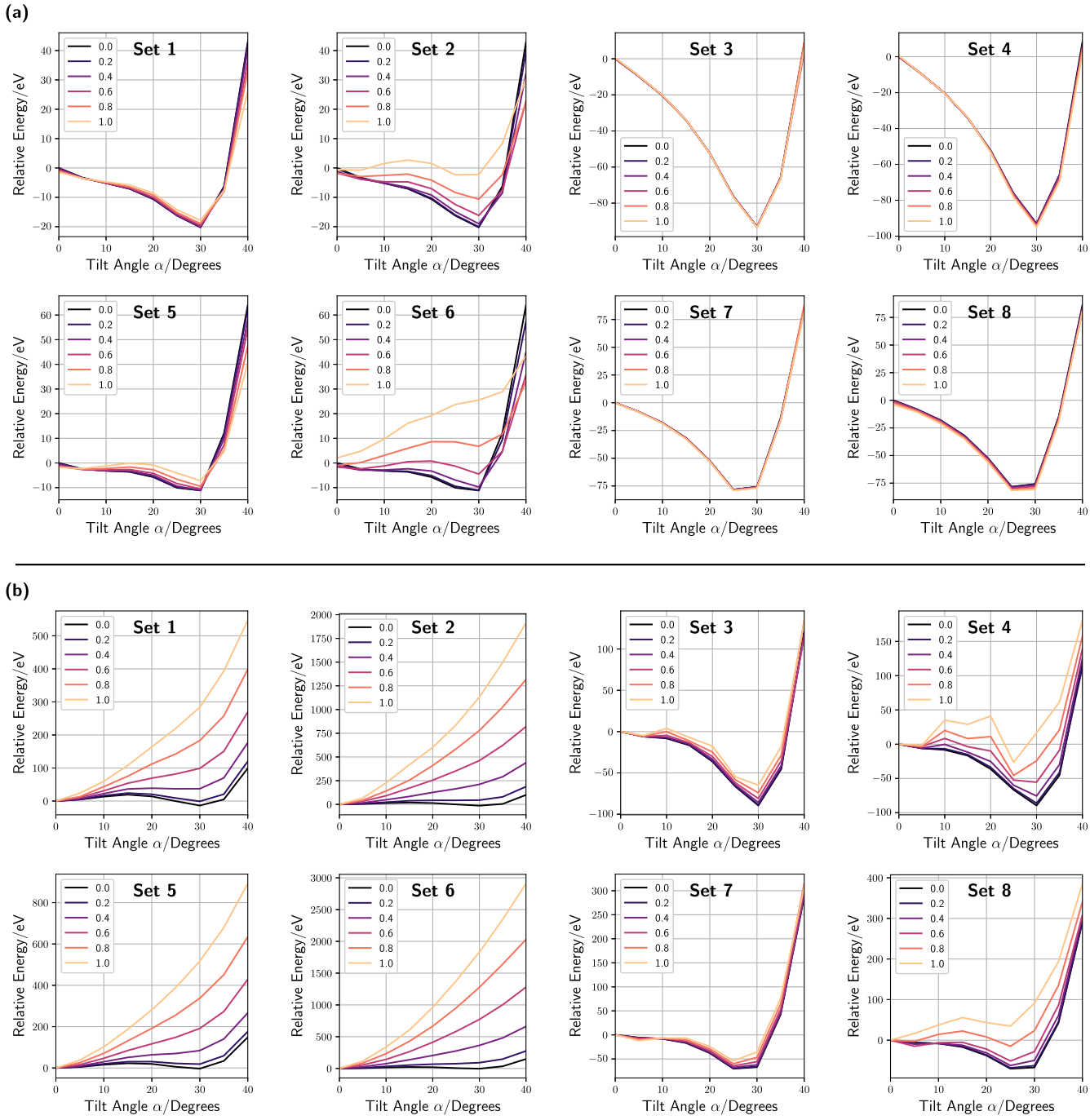

FIG. 4. Ligand tilt angle analysis for HDT^{H} on Au(111) at a density of 4.67 nm^{-2}. Pairwise interaction energies (a) and total energies (b) against ligand tilt angle α for different charge damping factors.

C. Tilt angle analysis on Au(111)

Having confirmed that the LJ components are primarily responsible for determining the tilt angles α, we now examine in more detail the HDT^{H} SAM on Au(111) at a surface density of 4.67 nm^{-2}, the highest of the two densities considered. Figure 4 presents the energy profiles, showing both the pairwise interaction and the total energy as functions of the tilt angle α for each of the FF sets listed in Table I. These profiles have been analyzed for different charge damping factors, ranging from 0 (fully damped, i.e., all atomic partial charges are equal to zero) to 1 (undamped).

To allow a clear comparison between the different FF sets and charge damping, the total energy curves for each set [Fig. 4(b)] were normalized to their respective values at α = 0°. Similarly, the pairwise interaction energy curves for all FF sets [Fig. 4(a)] have been calculated with respect to the values at α = 0° with a zero charge damping factor. This normalization ensures that variations in the energy profiles can be directly attributed to the changes in tilt angle α and the influence of the charge damping factor.

The first notable observation is the dependence of the pairwise interactions on the partial charges, which is evident for sets **1**, **2**, **5**, and **6**. This is demonstrated by the lack of superposition in the pairwise interaction energy scans across different charge damping factors for these sets. This is more pronounced for sets **2** and **6**. In contrast, sets **3**, **4**, **7**, and **8** exhibit pairwise energy profiles that are nearly identical across different damping factors, indicating a better separation of nonbonded parameter effects.

This dependence suggests an undesirable coupling between the nonbonded parameters, particularly the Coulomb and LJ interactions, which should ideally behave as independently additive in the CHARMM framework. The main source of this artifact appears to be the choice of LJ parameters. The sets employing UFF LJ parameters (i.e., sets **3**, **4**, **7**, and **8**) show minimal or no coupling, effectively mitigating this issue. Conversely, sets without UFF LJ parameters fail to decouple the interactions, resulting in distorted energy profiles.

The strength of this dependence is further influenced by the values of the partial charges used. Sets utilizing NBO partial charges show a stronger dependence on the charge damping factor than those using CGenFF charges. Even among sets with UFF LJ parameters, such as sets **7** and **8**, a slight residual dependence remains when NBO charges are used. These results highlight the critical interplay between the parameterization of partial charges and LJ potentials and emphasize the superior performance of combinations that minimize this coupling.

Looking now at the total energies [Fig. 4(b)], Coulomb repulsion dominates the behavior of set **1** (Fig. 3), most likely because at larger tilt angles the chains are oriented so that their charged sites are located closer together. Without appropriately chosen LJ parameters to buffer these interactions, electrostatic forces become the primary factor increasing the total energy. This pattern is similarly observed in sets **2**, **5**, and **6**, where the energy rises steeply with increasing angle. The effect is even more pronounced in sets **5** and **6**, which rely on NBO partial charges that are larger in absolute value than those provided by CGenFF for the hydrocarbon chain atoms (see Table S2). Consequently, the electrostatic repulsion is enhanced, leading to higher total energies. In contrast, sets **3**, **4**, **7**, and **8**—especially those with UFF LJ parameters—mitigate the dominance of Coulomb repulsion, resulting in more stable energy profiles. Although systems with NBO charges in this group (sets **4** and **8**) still exhibit greater variation when the charge damping factor is varied, their overall energetic behavior remains less sensitive to angle changes compared to the sets without UFF parameters.

It is evident at this stage that the sets with UFF LJ parameters consistently outperform the other parameter sets. The non-UFF LJ sets exhibit shallow minima in their pairwise interaction energy curves, sometimes accompanied by slight energy barriers between 0° and 30°. These shallow minima and barriers suggest a lack of adequate stabilization for the ligand tilt angle, which is critical for accurate modeling of the system. In contrast, the UFF LJ parameter sets (sets **3**, **4**, **7**, and **8**) exhibit well-defined and significantly deeper minima, free of such barriers, providing a much more stable and physically realistic description of the system. This trend is reflected most clearly in the total energy profiles, especially for sets **3** and **7**, further confirming the superiority of the UFF LJ parameters and the inadequacy of the NBO partial charges.

Among the UFF LJ sets, those with bonded parameters derived from CGenFF (sets **3** and **4**) exhibit particularly deep and sharp minima around 30°, which closely match the experimental observations.[15,16,21,22] This suggests that the combination of UFF LJ parameters and CGenFF bonded parameters provides a more reliable description of the ligand tilt angle and its associated energy landscape for the considered molecules. The use of NBO partial charges (as in sets **4** and **8**) introduces some instability and variation, particularly in response to charge damping, and obscures the energy minimum around 30°. Thus, set **3**, which integrates UFF LJ parameters with CGenFF charges, emerges as the most robust and accurate choice for describing the system.

The conclusions drawn from the analysis of HDT^{H} are largely applicable to the HDT^{OH} and HDT^{COOH} ligands, although some minor differences are observed (see Figs. S20 and S22). For HDT^{OH} (Fig. S22), the interference between Coulomb and LJ potentials is significantly reduced in sets **5** and **6**. This reduction is evident in the LJ energy profiles and becomes particularly clear in the total energy curves, which show a less steep increase at higher tilt angles than is observed for HDT^{H}. This improvement suggests that the interaction balance in these sets is better suited for hydroxyl-terminated ligands. Set **3** again emerges as the best descriptor among its peers.

Similar energy profiles have been observed for HDT^{COOH}, and a less steep increase in total energy occurs for non-UFF sets, although all of them present a barrier between 0° and 30°, as well as shallow minima at 30°. This effect is most likely due to inter-chain interactions between the carboxyl groups, which introduce additional complexity to the system. Interestingly, sets **3**, **4**, and **8** show slight interactions between LJ and Coulomb potentials that were not observed for the other ligands. These anomalies highlight the possible need to refine the parameters associated with the carboxyl group to achieve a more consistent description. Once again, set **3** offers the best performance over all others.

D. Tilt angle analysis on Au(100)

A similar investigation was carried out for the SAMs on Au(100) at a density of 4.17 nm^{-2}, the lowest of the two densities tested. The results for the HDT^{H} ligand are depicted in Fig. 5. The general conclusions drawn from the analysis of the

SAMs on Au(111) largely apply to this case as well. However, two notable differences emerge. First, the energy profiles for Au(100) have generally less pronounced minima, approaching a more parabolic shape. This is in contrast to the sharper, V-shaped curves observed for Au(111). Second, the equilibrium tilt angle for the ligands on Au(100) is smaller than that for Au(111). This result is consistent with the experimental characterizations discussed in Sec. I.

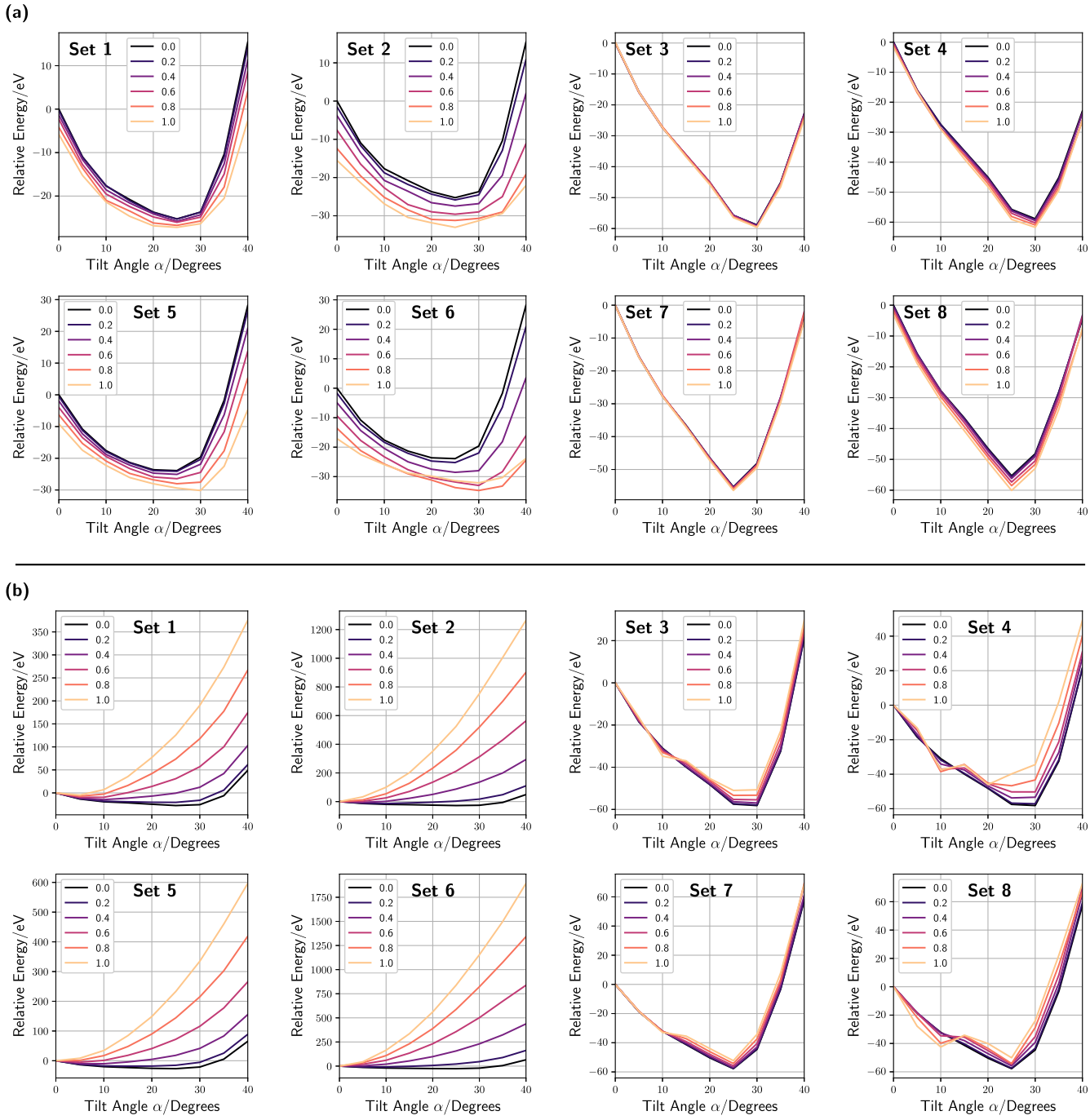

FIG. 5. Ligand tilt angle analysis for HDT^{H} on Au(100) at a density of 4.17 nm^{-2}. Pairwise interaction energies (a) and total energies (b) against ligand tilt angle α for different charge damping factors.

The less pronounced minima observed for Au(100) correlate with the lack of experimental consensus on the precise values of α for alkanethiol SAMs on this surface. This ambiguity likely reflects the inherent structural flexibility and variability of the SAMs on the Au(100) surface, in contrast to the more ordered arrangements on Au(111).

The differences in behavior between the different ligands for SAMs on Au(111) discussed previously are similarly observed for SAMs on Au(100), with significantly more distortion in the energy profiles for sets using NBO partial charges in the case of HDT^{COOH}. These variations highlight the influence of terminal group interactions and chain organization on the energy profiles and tilt angle distributions. Further details of these differences are shown in Figs. S18 and S20.

E. Influence of surface coverage density

Next, we evaluate the impact of surface coverage on the morphology of SAMs by analyzing different coverage densities on Au(100) and Au(111) surfaces. We considered two other cases: a

FIG. 6. Final HDT^{H} SAM model on Au(111) surface after 3 000 000 optimization steps. The initial geometry replicates the $\left(\sqrt{3} \times \sqrt{3}\right)$ R30° adsorption pattern and $c(4 \times 2)$ superlattice packing, consistent with structure III from Zhang, Goddard, and Jiang.[21] Blue spheres: carbon; yellow spheres: sulfur; and black, gray, and white spheres: top, middle, and bottom gold layers, respectively. (a) Evolution of the ligand tilt angle α during the optimization and (b) evolution of the precession (azimuthal) angle β during the optimization. In both cases, solid lines show the mean values, while shaded areas represent the one (orange) and two (yellow) standard deviations. (c) Histogram of the twist angles ω after optimization. (d) Top and side orthographic projections, along with a perspective view, which illustrate the final system's geometry. The inset in (d) provides a closer view of the sulfur atom arrangement, showing only the carbon atoms directly attached to the sulfurs for clarity. Hydrogen atoms and the two bottommost gold layers are omitted for clarity. The edges of the system were trimmed for clearer visualization.

slightly higher density of 4.73 nm^{-2} for Au(100) and a slightly lower density of 4.21 nm^{-2} for Au(111). These densities are compared with the experimentally measured value of 4.67 nm^{-2} for Au(111). For all cases, the total and pairwise interaction energies increase steeply as the ligand tilt angle α deviates from its low equilibrium value (see Figs. S15–S17 and S24–S26).

This behavior suggests that densities deviating from an optimum value, whether *higher* or *lower*, disrupt the intermolecular interactions responsible for maintaining the molecular tilt angle. In both scenarios, Coulomb repulsion prevails, undermining tilt stability. At higher density, this occurs because the ligands are too closely packed, causing repulsion that overrides the stabilization provided by the LJ interaction. Conversely, at lower density, the increased spacing prevents effective short-range LJ stabilization.

While the optimal density for Au(111) (i.e., the density that correctly reproduces the ligand tilt angle) is close to the experimental value, the optimal density for Au(100) exceeds the experimental benchmark for Au(111) by 0.06 nm^{-2}. Furthermore, despite its simple construction, the regular rectangular deposition does not capture the experimentally observed packing patterns, including the hexagonal sulfur arrangement and the superlattice formation of ligand chains, as shown in Fig. 1(b). Therefore, in Sec. III F, we discuss the results of simulations based on initial deposition patterns that explicitly reproduce the experimentally observed features of alkanethiol SAMs on Au(111) [Fig. 1(b)].

F. Final deposition geometry on Au(111)

From the evaluation of the FF parameter sets, set **3** consistently demonstrated superior performance compared to other configurations. Consequently, all subsequent analyses were carried out using set **3** to further investigate its ability to reproduce the experimental morphological features of SAMs. To test its predictive ability, an initial geometry was constructed based on experimental observations, incorporating the hexagonal $\left(\sqrt{3}\times\sqrt{3}\right)$ R30° arrangement of sulfur atoms and the $c(4\times2)$ superlattice packing of the ligand chains [see Fig. 1(b)]. These arrangements, corresponding to structure III from Zhang, Goddard, and Jiang,[21] were not spontaneously obtained from the initial rectangular grid arrangement but have been shown in previous studies to stabilize when explicitly used as the starting geometry.

Pool *et al.*[70] provided LJ parameters for sulfur atoms that demonstrated superior performance in a previous comparative study on the effect of sulfur LJ parameters on alkanethiol adsorption sites on gold.[42] Substitution of these parameters into set **3** resulted in an improvement in structural predictions. Thus, we substituted the original sulfur UFF parameters for these, attaining a slight overall improvement. The results of the MM optimization are summarized in Fig. 6. The optimized geometry achieves an average tilt angle of $\alpha \approx 35^\circ$ [Fig. 6(a)] and an azimuthal angle of $\beta \approx 60^\circ$ [Fig. 6(b)]. The dispersion of these angles, shown by the shaded areas in the plots, is very small. The bimodal distribution of ω angles is centered at the values of $\omega \approx -25^\circ$ and -55°, corresponding to the nearest-neighbor and third nearest-neighbor Au directions, respectively [Fig. 6(c)]. These results are in good agreement with experimental data and the results obtained from Zhang, Goddard, and Jiang,[21] underlining the effectiveness of the parameter set. The side and perspective views of the final geometry in Fig. 6(d) clearly show the characteristic chain tilt angle, as well as the relative twist angle ω between the chains. The top view also shows the uniformity of the precession angle across the surface, as evidenced in Fig. 6(b). The inset provides a focused view of the sulfur head-group arrangement by isolating the first carbon atoms directly connected to the sulfurs. This representation confirms the stability of the $\left(\sqrt{3}\times\sqrt{3}\right)$ R30° hexagonal arrangement and the formation of the $c(4\times2)$ superlattice shown in Fig. 1(b), both of which are consistent with experimentally observed patterns.

G. Preliminary molecular dynamics simulations

This work focuses primarily on the impact of force field parameters on the energetic and structural properties of alkanethiol SAMs. A detailed analysis of the dynamical behavior of these systems is reserved for a follow-up investigation. However, omitting the dynamical results would leave this study incomplete, since the final parameter set must produce not only a stable, optimized geometry but also structural integrity and stability at finite temperatures. As shown in the optimization analysis above, partial charges significantly influence the total energy landscape, occasionally counteracting the van der Waals interactions and altering the depth and shape of the energy minima (see Fig. 4). Although these effects were mitigated in the selected parameter set, the inclusion of thermal energy could still destabilize the system depending on the energy profile, potentially necessitating further fine-tuning of the partial charges.

To assess this aspect, we conducted a preliminary 10 ns MD simulation at 300 K for the HDT^H SAM, starting from the optimized geometry presented in Sec. III F. As anticipated, we observed an additional impact of the partial charges on structural features at finite temperatures. We, therefore, conducted additional simulations with uniformly scaled charges, using a damping increment of 0.1. A uniform scaling factor of 0.7 (i.e., 30% damping of the original values) was the minimal adjustment required to maintain the tilt angle near the experimental value of 30°. Further reduction of the partial charges had a negligible effect on the overall structural ordering. We then further refined this analysis from 0.700 to 0.800 in steps of 0.025, obtaining the same stability observed at 0.7 up to 0.725, finally setting that as the optimum value (further details can be found in the supplementary material).

In addition to the structural properties, another important property of SAM systems is their adsorption energy. Experimental estimates place the Au–S binding energy on Au(111) at ~44 kcal mol^{-1}, based on temperature-programmed desorption data.[71] Interchain interactions are estimated to contribute an additional 1–2 kcal mol^{-1} per methylene group.[16,30] The final optimized geometry obtained with our selected FF parameters, including the adjusted partial charges, yields a total adsorption energy of −61 kcal mol^{-1}, which falls within the expected range when both Au–S binding and interchain contributions are taken into account.

Through these investigations, we have successfully identified a set of force field parameters capable of accurately reproducing the experimentally observed features and previously reported computational results for three alkanethiol SAMs on Au(111). While the lack of well-defined structural data in the literature prevented explicit investigation of SAMs on Au(100), we expect the derived parameter set to reliably describe these systems as well. The strategy employed here can be extended to other functionalized alkanethiols, with different chain lengths and adsorbed on different surfaces.

The complete final parameter sets are provided in the supplementary material as ready-to-use files (Table S4). The final PSF files presented in the supplementary material already include the correction to the partial charges.

IV. CONCLUSIONS AND OUTLOOK

In this paper, we propose and demonstrate a systematic approach to evaluate how bonded interactions, atomic charges, and Lennard-Jones (LJ) parameters affect the geometrical and energetic characteristics of both pristine and functionalized alkanethiol SAMs on Au(100) and Au(111). To this end, we have performed an energy decomposition analysis as a function of the ligand tilt angle, which isolates the influence of each parameter on the overall behavior of the SAM. Application of this framework allowed us to identify that the force field set combining CGenFF bonded parameters and charges with UFF LJ parameters consistently delivers superior performance, reproducing experimentally observed structural and energetic features with high accuracy. The LJ parameters effectively govern the equilibrium tilt angle of the alkanethiol chains, allowing the formation of well-defined energy minima that closely match experimental data, particularly for Au(111). This parameterization also mitigates undesirable coupling between Coulomb and van der Waals interactions, enhancing the consistency and reliability of the model. The inclusion of carboxyl and hydroxyl ligands in our study addresses a notable limitation in the literature, which has mainly focused on unfunctionalized ligands in molecular-mechanics modeling of alkanethiol SAMs. Furthermore, our approach also paves the way for detailed investigations into the effect of varying surface nature, orientation, and ligand chain length.

Further analysis of surface coverage density and ligand packing reveals that simplistic rectangular grid arrangements inadequately capture the complexity of SAM organization. A configuration reflecting the experimentally observed $\left(\sqrt{3}\times\sqrt{3}\right)$ R30° hexagonal head-group arrangement and the $c(4\times2)$ superlattice patterns stabilizes the system at realistic adsorption sites and chain orientations. The chosen parameter set effectively reproduces key experimental trends, including the distinct structural behaviors observed on Au(111) and Au(100). The systematically validated framework presented here provides an effective model for the simulation of SAM-coated substrates. The validation of the parameterization over a range of ligands, densities, and lattice arrangements provides a basis for improving the predictive power of the simulations.

In recent years, complex many-body potentials, such as the charge-optimized many-body (COMB) framework,[72] and reactive potentials, such as ReaxFF[47,48] and rCHARMM,[73] have been developed to model various metal–ligand systems. Recent advances in machine-learned interatomic potentials (MLIPs) have further expanded the capabilities for modeling metal–ligand systems, including Au–S interactions. MLIP methods such as the Spectral Neighbor Analysis Potential (SNAP)[74] and DeePMD-kit[75] have demonstrated high accuracy across a variety of chemical environments. However, existing MLIPs are typically trained on small-molecule systems or ligand-protected nanoparticles,[76,77] and their direct applicability to densely packed, functionalized SAMs on extended crystalline gold surfaces remains limited. Moreover, incorporating such models into large-scale simulations that can resolve long-range ordering, surface patterning, and interchain interactions remains challenging, both computationally and in terms of practical implementation. In contrast, the classical parameter refinement strategy presented in this work provides a chemically interpretable, computationally efficient, and readily deployable alternative that is fully compatible with established simulation frameworks. A systematic comparison between classical and machine-learned approaches—once the latter are adapted to SAM environments—would represent a valuable direction for future research.

The results of this study provide a basis for further investigation of irradiation-driven chemistry in SAMs using the reactive CHARMM force field[73] and the irradiation-driven molecular dynamics method[78] implemented in the MBN Explorer software.[49] Together, these computational methods and tools can be used for multiscale modeling of different physicochemical phenomena ranging from the chemistry of adsorbed precursors to irradiation-induced transformations,[79,80] thus enabling atomistic simulations of SAM-mediated irradiation-driven processes. One such example is photoassisted chemical vapor deposition, in which SAMs act as substrates for metal deposition from light-activated precursors introduced in the gas phase. The modeling of this process will be the subject of our future studies.

SUPPLEMENTARY MATERIAL

The supplementary material includes the full set of results for the ligand tilt angle energy decomposition analysis for all three ligands and two densities on both Au(111) and Au(100), along with additional methodological details and links to the relevant simulation files (geometries, topologies, and force field parameters) referenced in this paper.

ACKNOWLEDGMENTS

This work was supported by the Engineering and Physical Sciences Research Council (Grant No. EP/W52461X/1). The financial support was provided by the European Commission through the RADON project (Grant Agreement No. 872494) within the H2020-MSCA-RISE-2019 program. This article is also based on work conducted as part of COST Action CA20129 "Multiscale Irradiation and Chemistry Driven Processes and Related Technologies" (MultIChem), supported by COST (European Cooperation in Science and Technology). C.P.S. and F.F. gratefully acknowledge the specialist and high-performance computing systems provided by Information Services at the University of Kent. Special thanks are extended to Dr. Timothy Kinnear for his invaluable assistance with high-performance computing resources.

AUTHOR DECLARATIONS

Conflict of Interest

The authors have no conflicts to disclose.

Author Contributions

Cauê P. Souza: Conceptualization (equal); Data curation (equal); Formal analysis (equal); Investigation (equal); Methodology (equal);

Software (equal); Validation (equal); Visualization (equal); Writing – original draft (equal); Writing – review & editing (equal). **Alexey V. Verkhovtsev**: Funding acquisition (equal); Methodology (equal); Resources (equal); Software (equal); Supervision (equal); Validation (supporting); Writing – original draft (equal); Writing – review & editing (equal). **Nigel J. Mason**: Funding acquisition (equal); Resources (equal); Supervision (equal); Writing – review & editing (equal). **Andrey V. Solov'yov**: Funding acquisition (equal); Resources (equal); Software (equal); Supervision (equal); Writing – review & editing (equal). **Felipe Fantuzzi**: Conceptualization (equal); Funding acquisition (equal); Methodology (equal); Project administration (equal); Resources (equal); Supervision (equal); Writing – original draft (equal); Writing – review & editing (equal).

DATA AVAILABILITY

The data that support the findings of this study are available within the article and its supplementary material. Additional data are available from the corresponding author upon reasonable request.

REFERENCES

[1] W. C. Bigelow, D. L. Pickett, and W. A. Zisman, "Oleophobic monolayers: I. Films adsorbed from solution in non-polar liquids," J. Colloid Sci. **1**, 513–538 (1946).

[2] V. M. Mirsky, "New electroanalytical applications of self-assembled monolayers," TrAC, Trends Anal. Chem. **21**, 439–450 (2002).

[3] D. Mandler and S. Kraus-Ophir, "Self-assembled monolayers (SAMs) for electrochemical sensing," J. Solid State Electrochem. **15**, 1535–1558 (2011).

[4] N. K. Chaki and K. Vijayamohanan, "Self-assembled monolayers as a tunable platform for biosensor applications," Biosens. Bioelectron. **17**, 1–12 (2002).

[5] S. K. Arya, P. R. Solanki, M. Datta, and B. D. Malhotra, "Recent advances in self-assembled monolayers based biomolecular electronic devices," Biosens. Bioelectron. **24**, 2810–2817 (2009).

[6] J. H. Schön, H. Meng, and Z. Bao, "Self-assembled monolayer organic field-effect transistors," Nature **413**, 713–716 (2001).

[7] M. Halik and A. Hirsch, "The potential of molecular self-assembled monolayers in organic electronic devices," Adv. Mater. **23**, 2689–2695 (2011).

[8] S. Casalini, C. A. Bortolotti, F. Leonardi, and F. Biscarini, "Self-assembled monolayers in organic electronics," Chem. Soc. Rev. **46**, 40–71 (2017).

[9] M. Singh, N. Kaur, and E. Comini, "The role of self-assembled monolayers in electronic devices," J. Mater. Chem. C **8**, 3938–3955 (2020).

[10] S. T. Marshall, M. O'Brien, B. Oetter, A. Corpuz, R. M. Richards, D. K. Schwartz, and J. W. Medlin, "Controlled selectivity for palladium catalysts using self-assembled monolayers," Nat. Mater. **9**, 853–858 (2010).

[11] C. A. Schoenbaum, D. K. Schwartz, and J. W. Medlin, "Controlling the surface environment of heterogeneous catalysts using self-assembled monolayers," Acc. Chem. Res. **47**, 1438–1445 (2014).

[12] J. Aizenberg, A. J. Black, and G. M. Whitesides, "Control of crystal nucleation by patterned self-assembled monolayers," Nature **398**, 495–498 (1999).

[13] A. Kumar, H. A. Biebuyck, and G. M. Whitesides, "Patterning self-assembled monolayers: Applications in materials science," Langmuir **10**, 1498–1511 (1994).

[14] N. K. Chaki, M. Aslam, J. Sharma, and K. Vijayamohanan, "Applications of self-assembled monolayers in materials chemistry," J. Chem. Sci. **113**, 659–670 (2001).

[15] J. C. Love, L. A. Estroff, J. K. Kriebel, R. G. Nuzzo, and G. M. Whitesides, "Self-assembled monolayers of thiolates on metals as a form of nanotechnology," Chem. Rev. **105**, 1103–1170 (2005).

[16] C. Vericat, M. E. Vela, G. Benitez, P. Carro, and R. C. Salvarezza, "Self-assembled monolayers of thiols and dithiols on gold: New challenges for a well-known system," Chem. Soc. Rev. **39**, 1805–1834 (2010).

[17] R. G. Nuzzo and D. L. Allara, "Adsorption of bifunctional organic disulfides on gold surfaces," J. Am. Chem. Soc. **105**, 4481–4483 (1983).

[18] K. R. Johnson, P. Arevalo Rodriguez, C. R. Brewer, J. A. Brannaka, Z. Shi, J. Yang, B. Salazar, L. McElwee-White, and A. V. Walker, "Photochemical CVD of Ru on functionalized self-assembled monolayers from organometallic precursors," J. Chem. Phys. **146**, 052816 (2016).

[19] B. G. Salazar, H. Liu, A. V. Walker, and L. McElwee-White, "Low temperature platinum chemical vapor deposition on functionalized self-assembled monolayers," J. Vac. Sci. Technol., A **38**, 033404 (2020).

[20] B. G. Salazar, C. R. Brewer, L. McElwee-White, and A. V. Walker, "Photoactivated Ru chemical vapor deposition using (η^3-allyl)$Ru(CO)_3X$ (X = Cl, Br, I): From molecular adsorption to Ru thin film deposition," J. Vac. Sci. Technol., A **40**, 023404 (2022).

[21] L. Zhang, W. A. Goddard III, and S. Jiang, "Molecular simulation study of the c(4×2) superlattice structure of alkanethiol self-assembled monolayers on Au(111)," J. Chem. Phys. **117**, 7342–7349 (2002).

[22] A. Ulman, "Formation and structure of self-assembled monolayers," Chem. Rev. **96**, 1533–1554 (1996).

[23] P. Fenter, A. Eberhardt, K. S. Liang, and P. Eisenberger, "Epitaxy and chain-length dependent strain in self-assembled monolayers," J. Chem. Phys. **106**, 1600–1608 (1997).

[24] J. Hautman and M. L. Klein, "Molecular dynamics simulation of the effects of temperature on a dense monolayer of long-chain molecules," J. Chem. Phys. **93**, 7483–7492 (1990).

[25] C. D. Bain, E. B. Troughton, Y. T. Tao, J. Evall, G. M. Whitesides, and R. G. Nuzzo, "Formation of monolayer films by the spontaneous assembly of organic thiols from solution onto gold," J. Am. Chem. Soc. **111**, 321–335 (1989).

[26] H. Gojzewski, M. Kappl, and A. Ptak, "Effect of the chain length and temperature on the adhesive properties of alkanethiol self-assembled monolayers," Langmuir **33**, 11862–11868 (2017).

[27] R. Desikan, S. Armel, H. M. Meyer III, and T. Thundat, "Effect of chain length on nanomechanics of alkanethiol self-assembly," Nanotechnology **18**, 424028 (2007).

[28] M. D. Malinsky, K. L. Kelly, G. C. Schatz, and R. P. Van Duyne, "Chain length dependence and sensing capabilities of the localized surface plasmon resonance of silver nanoparticles chemically modified with alkanethiol self-assembled monolayers," J. Am. Chem. Soc. **123**, 1471–1482 (2001).

[29] B. Wang, J. Luo, X. Wang, H. Wang, and J. G. Hou, "Dielectric properties and frequency response of self-assembled monolayers of alkanethiols," Langmuir **20**, 5007–5012 (2004).

[30] F. Schreiber, "Structure and growth of self-assembling monolayers," Prog. Surf. Sci. **65**, 151–257 (2000).

[31] R. G. Nuzzo, L. H. Dubois, and D. L. Allara, "Fundamental studies of microscopic wetting on organic surfaces. 1. Formation and structural characterization of a self-consistent series of polyfunctional organic monolayers," J. Am. Chem. Soc. **112**, 558–569 (1990).

[32] G. E. Poirier, M. J. Tarlov, and H. E. Rushmeier, "Two-dimensional liquid phase and the px.sqroot.3 phase of alkanethiol self-assembled monolayers on Au(111)," Langmuir **10**, 3383–3386 (1994).

[33] H. Sellers, A. Ulman, Y. Shnidman, and J. E. Eilers, "Structure and binding of alkanethiolates on gold and silver surfaces: Implications for self-assembled monolayers," J. Am. Chem. Soc. **115**, 9389–9401 (1993).

[34] L. Strong and G. M. Whitesides, "Structures of self-assembled monolayer films of organosulfur compounds adsorbed on gold single crystals: Electron diffraction studies," Langmuir **4**, 546–558 (1988).

[35] N. Camillone III, C. E. D. Chidsey, G.-y. Liu, and G. Scoles, "Substrate dependence of the surface structure and chain packing of docosyl mercaptan self-assembled on the (111), (110), and (100) faces of single crystal gold," J. Chem. Phys. **98**, 4234–4245 (1993).

[36] L. H. Dubois, B. R. Zegarski, and R. G. Nuzzo, "Molecular ordering of organosulfur compounds on Au(111) and Au(100): Adsorption from solution and in ultrahigh vacuum," J. Chem. Phys. **98**, 678–688 (1993).

[37] P. Maksymovych, D. C. Sorescu, and J. T. Yates, "Methanethiolate adsorption site on Au(111): A combined STM/DFT study at the single-molecule level," J. Phys. Chem. B **110**, 21161–21167 (2006).

[38]T. T. Järvi, A. C. T. van Duin, K. Nordlund, and W. A. Goddard III, "Development of interatomic ReaxFF potentials for Au–S–C–H systems," J. Phys. Chem. A **115**, 10315–10322 (2011).
[39]Y. Ahn, J. K. Saha, G. C. Schatz, and J. Jang, "Molecular dynamics study of the formation of a self-assembled monolayer on gold," J. Phys. Chem. C **115**, 10668–10674 (2011).
[40]H. Häkkinen, "The gold–sulfur interface at the nanoscale," Nat. Chem. **4**, 443–455 (2012).
[41]D. Stefanakis, V. Harmandaris, G. Kopidakis, and I. Remediakis, "From order to disorder of alkanethiol self-assembled monolayers on complex Au (211), (221), and (311) surfaces: Impact of the Substrate," J. Phys. Chem. C **125**, 3495–3508 (2021).
[42]T. Djebaili, S. Abel, M. Marchi, and J. Richardi, "Influence of force-field parameters on the atomistic simulations of metallic surfaces and nanoparticles," J. Phys. Chem. C **121**, 27758–27765 (2017).
[43]T.-W. Li, I. Chao, and Y.-T. Tao, "Relationship between packing structure and headgroups of self-assembled monolayers on Au(111): Bridging experimental observations through computer simulations," J. Phys. Chem. B **102**, 2935–2946 (1998).
[44]R. Bhatia and B. J. Garrison, "Structure of c(4×2) superlattice in alkanethiolate self-assembled monolayers," Langmuir **13**, 4038–4043 (1997).
[45]J. J. Gerdy and W. A. Goodard, "Atomistic structure for self-assembled monolayers of alkanethiols on Au(111) surfaces," J. Am. Chem. Soc. **118**, 3233–3236 (1996).
[46]A. K. Rappe, C. J. Casewit, K. S. Colwell, W. A. Goddard III, and W. M. Skiff, "UFF, a full periodic table force field for molecular mechanics and molecular dynamics simulations," J. Am. Chem. Soc. **114**, 10024–10035 (1992).
[47]A. C. T. van Duin, S. Dasgupta, F. Lorant, and W. A. Goddard, "ReaxFF: A reactive force field for hydrocarbons," J. Phys. Chem. A **105**, 9396–9409 (2001).
[48]T. P. Senftle, S. Hong, M. M. Islam, S. B. Kylasa, Y. Zheng, Y. K. Shin, C. Junkermeier, R. Engel-Herbert, M. J. Janik, H. M. Aktulga, T. Verstraelen, A. Grama, and A. C. T. van Duin, "The ReaxFF reactive force-field: Development, applications and future directions," npj Comput. Mater. **2**, 15011 (2016).
[49]I. A. Solov'yov, A. V. Yakubovich, P. V. Nikolaev, I. Volkovets, and A. V. Solov'yov, "MesoBioNano explorer—A universal program for multiscale computer simulations of complex molecular structure and dynamics," J. Comput. Chem. **33**, 2412–2439 (2012).
[50]G. B. Sushko, I. A. Solov'yov, and A. V. Solov'yov, "Modeling MesoBioNano systems with MBN studio made easy," J. Mol. Graphics Modell. **88**, 247–260 (2019).
[51]V. Zoete, M. A. Cuendet, A. Grosdidier, and O. Michielin, "SwissParam: A fast force field generation tool for small organic molecules," J. Comput. Chem. **32**, 2359–2368 (2011).
[52]M. Bugnon, M. Goullieux, U. F. Röhrig, M. A. S. Perez, A. Daina, O. Michielin, and V. Zoete, "SwissParam 2023: A modern web-based tool for efficient small molecule parametrization," J. Chem. Inf. Model. **63**, 6469–6475 (2023).
[53]K. Vanommeslaeghe, E. Hatcher, C. Acharya, S. Kundu, S. Zhong, J. Shim, E. Darian, O. Guvench, P. Lopes, I. Vorobyov, and A. D. Mackerell, Jr., "CHARMM general force field: A force field for drug-like molecules compatible with the CHARMM all-atom additive biological force fields," J. Comput. Chem. **31**, 671–690 (2010).
[54]K. Vanommeslaeghe and A. D. MacKerell, Jr., "Automation of the CHARMM general force field (CGenFF) I: Bond perception and atom typing," J. Chem. Inf. Model. **52**, 3144–3154 (2012).
[55]K. Vanommeslaeghe, E. P. Raman, and A. D. MacKerell, Jr., "Automation of the CHARMM general force field (CGenFF) II: Assignment of bonded parameters and partial atomic charges," J. Chem. Inf. Model. **52**, 3155–3168 (2012).
[56]W. L. Jorgensen, D. S. Maxwell, and J. Tirado-Rives, "Development and testing of the OPLS all-atom force field on conformational energetics and properties of organic liquids," J. Am. Chem. Soc. **118**, 11225–11236 (1996).
[57]L. S. Dodda, I. Cabeza de Vaca, J. Tirado-Rives, and W. L. Jorgensen, "LigParGen web server: An automatic OPLS-AA parameter generator for organic ligands," Nucleic Acids Res. **45**, W331–W336 (2017).
[58]P. Bhadra and S. W. I. Siu, "Comparison of biomolecular force fields for alkanethiol self-assembled monolayer simulations," J. Phys. Chem. C **121**, 26340–26349 (2017).
[59]Y. Zhao and D. G. Truhlar, "The M06 suite of density functionals for main group thermochemistry, thermochemical kinetics, noncovalent interactions, excited states, and transition elements: Two new functionals and systematic testing of four M06-class functionals and 12 other functionals," Theor. Chem. Acc. **120**, 215–241 (2008).
[60]S. Grimme, J. Antony, S. Ehrlich, and H. Krieg, "A consistent and accurate *ab initio* parametrization of density functional dispersion correction (DFT-D) for the 94 elements H-Pu," J. Chem. Phys. **132**, 154104 (2010).
[61]F. Weigend and R. Ahlrichs, "Balanced basis sets of split valence, triple zeta valence and quadruple zeta valence quality for H to Rn: Design and assessment of accuracy," Phys. Chem. Chem. Phys. **7**, 3297–3305 (2005).
[62]E. D. Glendening, C. R. Landis, and F. Weinhold, "Natural bond orbital methods," Wiley Interdiscip. Rev.: Comput. Mol. Sci. **2**, 1–42 (2012).
[63]M. J. Frisch, G. W. Trucks, H. B. Schlegel, G. E. Scuseria, M. A. Robb, J. R. Cheeseman, G. Scalmani, V. Barone, G. A. Petersson, H. Nakatsuji, X. Li, M. Caricato, A. V. Marenich, J. Bloino, B. G. Janesko, R. Gomperts, B. Mennucci, H. P. Hratchian, J. V. Ortiz, A. F. Izmaylov, J. L. Sonnenberg, D. Williams-Young, F. Ding, F. Lipparini, F. Egidi, J. Goings, B. Peng, A. Petrone, T. Henderson, D. Ranasinghe, V. G. Zakrzewski, J. Gao, N. Rega, G. Zheng, W. Liang, M. Hada, M. Ehara, K. Toyota, R. Fukuda, J. Hasegawa, M. Ishida, T. Nakajima, Y. Honda, O. Kitao, H. Nakai, T. Vreven, K. Throssell, J. A. Montgomery, Jr., J. E. Peralta, F. Ogliaro, M. J. Bearpark, J. J. Heyd, E. N. Brothers, K. N. Kudin, V. N. Staroverov, T. A. Keith, R. Kobayashi, J. Normand, K. Raghavachari, A. P. Rendell, J. C. Burant, S. S. Iyengar, J. Tomasi, M. Cossi, J. M. Millam, M. Klene, C. Adamo, R. Cammi, J. W. Ochterski, R. L. Martin, K. Morokuma, O. Farkas, J. B. Foresman, and D. J. Fox, *Gaussian 16, Revision A.03*, Gaussian, Inc., Wallingford, CT, 2016.
[64]M. W. Finnis and J. E. Sinclair, "A simple empirical N-body potential for transition metals," Philos. Mag. A **50**, 45–55 (1984).
[65]G. J. Ackland and R. Thetford, "An improved *N*-body semi-empirical model for body-centred cubic transition metals," Philos. Mag. A **56**, 15–30 (1987).
[66]P. K. Ghorai and S. C. Glotzer, "Molecular dynamics simulation study of self-assembled monolayers of alkanethiol surfactants on spherical gold nanoparticles," J. Phys. Chem. C **111**, 15857–15862 (2007).
[67]B. Quentrec and C. Brot, "New method for searching for neighbors in molecular dynamics computations," J. Comput. Phys. **13**, 430–432 (1973).
[68]R. T. McGibbon, K. A. Beauchamp, M. P. Harrigan, C. Klein, J. M. Swails, C. X. Hernández, C. R. Schwantes, L.-P. Wang, T. J. Lane, and V. S. Pande, "MDTraj: A modern open library for the analysis of molecular dynamics trajectories," Biophys. J. **109**, 1528–1532 (2015).
[69]J. D. Hunter, "Matplotlib: A 2D graphics environment," Comput. Sci. Eng. **9**, 90–95 (2007).
[70]R. Pool, P. Schapotschnikow, and T. J. H. Vlugt, "Solvent effects in the adsorption of alkyl thiols on gold structures: A molecular simulation study," J. Phys. Chem. C **111**, 10201–10212 (2007).
[71]L. H. Dubois and R. G. Nuzzo, "Synthesis, structure, and properties of model organic surfaces," Annu. Rev. Phys. Chem. **43**, 437–463 (1992).
[72]T. Liang, T.-R. Shan, Y.-T. Cheng, B. D. Devine, M. Noordhoek, Y. Li, Z. Lu, S. R. Phillpot, and S. B. Sinnott, "Classical atomistic simulations of surfaces and heterogeneous interfaces with the charge-optimized many body (COMB) potentials," Mater. Sci. Eng., R **74**, 255–279 (2013).
[73]G. B. Sushko, I. A. Solov'yov, A. V. Verkhovtsev, S. N. Volkov, and A. V. Solov'yov, "Studying chemical reactions in biological systems with MBN explorer: Implementation of molecular mechanics with dynamical topology," Eur. Phys. J. D **70**, 12 (2016).
[74]A. P. Thompson, L. P. Swiler, C. R. Trott, S. M. Foiles, and G. J. Tucker, "Spectral neighbor analysis method for automated generation of quantum-accurate interatomic potentials," J. Comput. Phys. **285**, 316–330 (2015).
[75]H. Wang, L. Zhang, J. Han, and W. E, "DeePMD-kit: A deep learning package for many-body potential energy representation and molecular dynamics," Comput. Phys. Commun. **228**, 178–184 (2018).
[76]C. A. McCandler, A. Pihlajamäki, S. Malola, H. Häkkinen, and K. A. Persson, "Gold–thiolate nanocluster dynamics and intercluster reactions enabled by a machine learned interatomic potential," ACS Nano **18**, 19014–19023 (2024).
[77]Y. Wang, D. S. N. D. Samarasinghe, H. Deng, B. Liu, and C. M. Aikens, "Gaussian process approach to constructing transferable force fields for thiolate-protected gold nanoclusters," J. Chem. Inf. Model. **65**, 3892–3902 (2025).

[78]G. B. Sushko, I. A. Solov'yov, and A. V. Solov'yov, "Molecular dynamics for irradiation driven chemistry: Application to the FEBID process," Eur. Phys. J. D **70**, 217 (2016).
[79]A. V. Solov'yov, A. V. Verkhovtsev, N. J. Mason, R. A. Amos, I. Bald, G. Baldacchino, B. Dromey, M. Falk, J. Fedor, L. Gerhards, M. Hausmann, G. Hildenbrand, M. Hrabovský, S. Kadlec, J. Kočišek, F. Lépine, S. Ming, A. Nisbet, K. Ricketts, L. Sala, T. Schlathölter, A. E. H. Wheatley, and I. A. Solov'yov, "Condensed matter systems exposed to radiation: Multiscale theory, simulations, and experiment," Chem. Rev. **124**, 8014–8129 (2024).
[80]A. V. Verkhovtsev, I. A. Solov'yov, and A. V. Solov'yov, "Irradiation-driven molecular dynamics: A review," Eur. Phys. J. D **75**, 213 (2021).